



HAL
open science

The structure of nitrogen-supersaturated ferrite produced by ball milling

Jochen Aufrecht, Andreas Leineweber, Eric Jan Mittemeijer, Jacques Foct

► **To cite this version:**

Jochen Aufrecht, Andreas Leineweber, Eric Jan Mittemeijer, Jacques Foct. The structure of nitrogen-supersaturated ferrite produced by ball milling. *Philosophical Magazine*, 2008, 88 (12), pp.1835-1855. 10.1080/14786430802322198 . hal-00513934

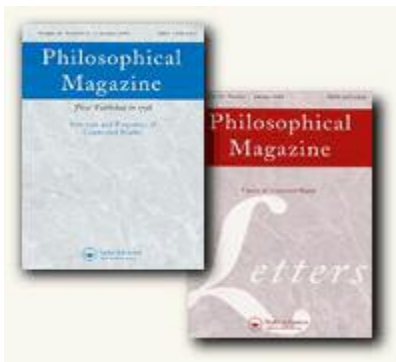
HAL Id: hal-00513934

<https://hal.science/hal-00513934>

Submitted on 1 Sep 2010

HAL is a multi-disciplinary open access archive for the deposit and dissemination of scientific research documents, whether they are published or not. The documents may come from teaching and research institutions in France or abroad, or from public or private research centers.

L'archive ouverte pluridisciplinaire **HAL**, est destinée au dépôt et à la diffusion de documents scientifiques de niveau recherche, publiés ou non, émanant des établissements d'enseignement et de recherche français ou étrangers, des laboratoires publics ou privés.



The structure of nitrogen-supersaturated ferrite produced by ball milling

Journal:	<i>Philosophical Magazine & Philosophical Magazine Letters</i>
Manuscript ID:	TPHM-08-May-0145.R1
Journal Selection:	Philosophical Magazine
Date Submitted by the Author:	30-Jun-2008
Complete List of Authors:	Aufrecht, Jochen; Max Planck Institute for Metals Research Leineweber, Andreas; Max Planck Institute for Metals Research, Department Mittemeijer Mittemeijer, Eric Jan; Max Planck Institute for Metals Research, Prof. Dr Ir. E.J. Mittemeijer Foct, Jacques; Laboratoire de Métallurgie Physique et Génie des Matériaux
Keywords:	ball-milling, lattice defects, Mossbauer spectroscopy, nanograined structures, nitrides, X-ray diffraction
Keywords (user supplied):	ball-milling, lattice defects, Mossbauer spectroscopy



The structure of nitrogen-supersaturated ferrite produced by ball milling

J. Aufrecht^a, A. Leineweber^{a*}, J. Foct^b, E.J. Mittemeijer^a

^aMax Planck Institute for Metals Research, Heisenbergstrasse 3, D-70569 Stuttgart, Germany; ^bLaboratoire de Métallurgie Physique et Génie des Matériaux, UMR CNRS 8517, Université des Sciences et Technologies de Lille, 59655 Villeneuve-d'Ascq Cedex, France

Highly supersaturated solid solutions of nitrogen in ferrite (bcc) were produced by ball milling of various powder mixtures of α -iron and ϵ -Fe₃N_{1.08}. The microstructure and the crystal structure of the product phases were examined as function of nitrogen content using X-ray powder diffraction, high-resolution electron microscopy and Mössbauer spectroscopy. It was found that the grain size decreases with increasing nitrogen content. Unexpected shifts of the reflections in the X-ray powder diffraction patterns of the supersaturated N-ferrites, depending on the hkl values of the reflections and nitrogen content, were observed. It could be shown that these shifts cannot be explained by tetragonal distortion of the bcc-unit cell, but they are in accordance with the occurrence of a certain type of stacking faults on bcc- $\{211\}$ planes. This result, together with the observation of some isolated fcc crystals (by high-resolution electron microscopy) and a drop in microstrain for high nitrogen contents, demonstrates that unconventional deformation mechanisms are operative in these materials below a certain grain size, leading to a breakdown of the classical Hall-Petch relation for mechanical strengthening.

Keywords: Ball milling, FeN alloys, X ray diffraction, Moessbauer, nanosrtructure

1. Introduction

Ball milling has attracted considerable attention in materials science in the last decades since it is a technique which for many systems, by a solid-to-solid route at room temperature, offers the possibility to produce non-equilibrium phases, e.g. severely distorted nanocrystalline

* Corresponding author. Email: a.leineweber@mf.mpg.de

1
2
3 phases, extended solid solutions, disordered intermetallic phases and amorphous alloys [1-6].
4
5 In the system Fe-N, ball-milling [7-22] in particular has been frequently discussed as a
6
7 possible synthetic route to produce single-phase α'' -Fe₁₆N₂, a nitrogen-ordered martensite-
8
9 like phase, which is claimed to possess unique magnetic properties [23], but has not been
10
11 produced as single-phase bulk material until now. Two other metastable Fe-N phases could be
12
13 produced via ball milling: (i) a solid solution of nitrogen in α -iron with a largely extended
14
15 nitrogen solubility (proposed symbol: α''' , [8]) up to about 16.5 at% nitrogen [9] (thus
16
17 comprising the Fe₁₆N₂ composition, i.e. 11.1 at% N), which is a multitude of the equilibrium
18
19 solubility of nitrogen in α -iron (0.4 at% at 592°C, [24]) and (ii) an iron-rich ϵ -iron nitride in a
20
21 temperature-composition window, within which the ϵ -nitride is thermodynamically unstable
22
23 with respect to transformation into γ' -Fe₄N or decomposition into γ' -Fe₄N and α -iron [24].
24
25 These metastable phases appear to form upon sufficiently long milling of α -iron in the
26
27 presence of a nitrogen source, independent of the type of nitrogen source whether it is solid
28
29 (iron nitrides, nitrogen containing organic compounds) [7-21] or gaseous (nitrogen, ammonia)
30
31 [16,17,22]; the type of phase formed appears to depend only on the total Fe/N ratio of the
32
33 reacting system.
34
35
36
37
38
39
40

41 Especially the solid solution of nitrogen in α -iron with a largely extended nitrogen
42
43 solubility has been subject of a number of investigations attempting to clarify the crystal-,
44
45 nano- and microstructure of this phase in relation with the unusually high nitrogen solubility
46
47 (up to 16.5 at%). Usually, the solubility of nitrogen (and other interstitially dissolved atoms)
48
49 is very low for bcc-type materials due to the irregular shape and limited size of the octahedral
50
51 interstitial sites which gives rise to considerable local, tetragonal lattice distortion upon
52
53 interstitially dissolving of nitrogen. X-ray powder diffraction (XRPD) patterns recorded from
54
55 such supersaturated N-ferrites show some unexpected features: the reflection profiles tend to
56
57 be asymmetric [16-19] and the lattice spacings calculated from the reflection maxima are too
58
59 small in view of the nitrogen content and the known dependency [25,26] of lattice parameter
60

1
2
3 on nitrogen content for α -Fe [17,20]. As explanation for the too small lattice-parameter
4 values, it was suggested that nitrogen segregates to defects, which are introduced in a large
5 number by ball milling [19], or even the occurrence of an amorphous nitrogen-rich grain-
6 boundary phase was postulated [20]. The asymmetric reflection broadening was ascribed to
7 the ferrite matrix on average being completely or partly tetragonally distorted [15-19],
8 implying preferred occupation by nitrogen of one of the three types of octahedral interstitial
9 sites, as in nitrogen martensite. This interpretation was rejected by other authors on the basis
10 of Mössbauer spectroscopy and electron diffraction data [8-10]. Furthermore, in one work [7],
11 it was noted in passing that a hkl -dependent reflection shift may occur with increasing
12 nitrogen content, which effect has not been investigated further and quantified until now.

13
14
15
16
17
18
19
20
21
22
23
24
25
26
27
28
29
30
31
32
33
34
35
36
37
38
39
40
41
42
43
44
45
46
47
48
49
50
51
52
53
54
55
56
57
58
59
60

The general difficulties in obtaining an unambiguous structure model of the supersaturated solid solution of nitrogen in α -iron, consistent with the experimental observations, is at least partly caused by the small crystallite size in combination with the high defect density which is result of the severe plastic deformation process via ball milling. This results in very broad Bragg reflections in X-ray powder-diffraction patterns, leading usually to a poor signal-to-noise ratio; also the use of optical or scanning-electron microscopy for microstructural investigations cannot provide adequate information.

The present work aims at improving the experimental data basis on the very strongly supersaturated solid solutions of N in α -Fe by preparing a series of α -Fe[N] alloys of a wide range of N content, by ball milling mixtures of pure Fe and ϵ -Fe₃N_{1.08}, which are investigated by accurate X-ray diffraction, Mössbauer spectroscopy and high-resolution transmission electron microscopy. Emphasis is laid on tracing changes in the diffraction patterns of the steady-state products with increasing nitrogen content, especially on deviations with respect to the diffraction pattern as expected for bcc-ferrite. It is checked whether these deviations can be aligned with the occurrence of overall tetragonal distortion of the ferrite. This possibility is

1
2
3 disproved. Then, an alternative microstructural model, based on the occurrence of a special
4 type of stacking faults, is proposed, which can explain the experimental results.
5
6
7
8
9

10 **2. Experimental procedure**

11 **2.1 *Ball milling***

12
13 As starting materials, mechanical mixtures of α -iron powder and ϵ -iron nitride powder were
14 used. The iron powder (Alfa Aesar) had a purity of 99.9 wt% with respect to the metal base
15 and a purity of 99.5 wt% considering also non-metallic impurities, the particle size was of less
16 than 10 μm . The ϵ -iron nitride powder was produced by gas nitriding of iron powder (3 \times 36 h
17 at 510°C in an ammonia/hydrogen atmosphere, applying a technical nitriding furnace (C.
18 Gommann KG, Remscheid, D, see also [27]). The ϵ -iron nitride powder had a final nitrogen
19 content of 26.5 at%. To prevent oxidation, the powders were stored in an argon-filled glove
20 box. The iron and ϵ -iron nitride powders were weighted-in in specified weight ratios to
21 establish a desired total nitrogen content in the powder mixtures and were mingled in a mortar
22 to realize a uniform initial intermixture. The resulting powder mixtures were filled into a
23 stainless steel vessel for milling together with stainless-steel milling balls of 10 mm diameter,
24 also in the argon-filled glove box to assure an inert atmosphere inside the vessel. The use of
25 about 7.2 g of powder mixture together with 35 milling balls resulted in a constant powder-to-
26 balls weight ratio of 1:20 for all experiments. The vessel was afterwards sealed by an o-ring
27 and additionally by parafilm. The powders were milled in a "Fritsch Pulverisette 6" planetary
28 ball mill at a rotational speed of 500 rpm for 40 h (effective milling time). Every 30 minutes,
29 the milling process was interrupted for 20 minutes to minimize the temperature raise during
30 milling. After each interruption, the direction of rotation was reversed.
31
32
33
34
35
36
37
38
39
40
41
42
43
44
45
46
47
48
49
50
51
52
53
54
55
56
57
58
59
60

2.2 *X-ray powder diffraction (XRPD)*

1
2
3 For one powder mixture (sample A5, see section 3 and table 2), the alloying process during
4 ball milling was traced as a function of milling time by XRPD measurements using a Guinier
5 camera “Enraf Nonius FR 552” applying Mo-K α_1 radiation ($\lambda=0.70926$ Å). To this end, a few
6 mg of sample material were removed from the vessel after certain milling times in the argon-
7 filled glove box. The amount of removed material was small enough to ensure that the ball-to-
8 powder weight ratio was not changed significantly.
9

10
11
12
13
14
15
16
17 The steady-state products as obtained after 40 h of ball milling in all experiments were
18 examined using an X’PERT Multi-Purpose-Diffractometer in θ - θ -Bragg-Brentano geometry,
19 employing Co-K α radiation ($\lambda_{\alpha 1}=1.78897$ Å, $\lambda_{\alpha 2}=1.79258$ Å) and using a monochromator in
20 the diffracted beam. For this purpose the powders were suspended in isopropanol and
21 sedimented on a (510)-cut Si crystal plate (wafer) using a supporting brass ring during
22 evaporation of the liquid.
23
24
25
26
27
28
29
30

31
32 The thus recorded diffraction patterns were analysed using the program TOPAS [28].
33 An instrumental-profile function was determined for the chosen diffractometer setting using a
34 LaB₆ powder (NIST standard reference material, SRM660a) employing the fundamental
35 parameters approach [29]; some parameters pertaining to certain instrumental-line profile
36 contributions like the wavelength-distribution function were allowed to be refined in the
37 fitting of the LaB₆ reflections. The instrumental profile thus obtained was convoluted with a
38 split pseudo-Voigt function for each single bcc-type reflection, using the programming
39 language available in the *Launch Mode* of TOPAS. By least-squares-fitting to the reflections
40 recorded from the ball-milled powders, the parameters peak maximum ($2\theta_{\max}$), full width at
41 half maximum (FWHM), asymmetry, intensity and mixing parameter of the pseudo-Voigt
42 functions were extracted for each single reflection (data in sections 3.2 – 3.4).
43
44
45
46
47
48
49
50
51
52
53
54
55
56
57
58
59
60

2.3 Chemical Analysis

1
2
3 The nitrogen content and the extent of oxygen contamination of the final products were
4 determined using carrier-gas hot extraction (ELTRA ONH 2000).
5
6
7
8
9

10 **2.4 Mössbauer spectroscopy**

11 Spectra were obtained at room temperature in transmission geometry with a Wissel driver
12 working in the constant acceleration mode in the velocity interval ($- 8, + 8 \text{ mm s}^{-1}$). The ^{57}Co
13 atoms of the 50 mC source are dissolved in a rhodium matrix.
14
15
16
17
18
19
20
21

22 **2.5 Transmission electron microscopy**

23 For high-resolution transmission electron microscopy (HRTEM) examinations, the powders
24 were mixed with an epoxy resin and put between two silicon discs, which are strengthened by
25 aluminum bars on top and on bottom. After hardening of the epoxy resin, cross-sectional
26 slices were cut from the package, which were dimpled and ion-thinned to achieve an electron
27 transparent sample thickness. The samples were examined with a JEOL-ARM 1250
28 transmission electron microscope applying an electron acceleration voltage of 1250 kV.
29
30
31
32
33
34
35
36
37
38
39
40

41 **3. Experimental results**

42 **3.1 Chemical composition of the as-milled samples**

43 Chemical analysis showed that no loss of nitrogen occurred during ball milling, see Table 2.
44 The slight increase in nitrogen content detected for most of the samples (compare Table 2 and
45 Table 1) is attributed to uptake of nitrogen from the atmosphere, which is unavoidable in the
46 ball milling experiment, despite the measures taken to prevent contamination by atmospheric
47 gases (cf. section 2.1). The same holds for the increase in oxygen content, which is expected
48 to lead to formation of oxides, which however were not detected by X-ray diffraction. Hence,
49 as the nitrogen content changed slightly during milling, the final (steady-state) N content in
50 the as-milled state, as determined by chemical analysis, will be referred to henceforth.
51
52
53
54
55
56
57
58
59
60

{Place Tables 1 and 2 about here}

3.2 Phase analysis

The evolution of the mechanical alloying process was traced for sample A5 as function of milling time using XRPD (Fig. 1). Already during the initial stages of milling, a strong broadening of the originally α -Fe and ϵ -reflections is induced, obviously caused by both severe plastic deformation and the associated reduction in crystallite size (cf. section 3.3). Also compositional variations due to nitrogen redistribution processes will contribute to the diffraction-line broadening. The reflections of the ϵ -nitride are no more detectable after several hours of milling. Obviously, under the mechanical activation by ball milling, the ϵ -nitride reacts with the α -iron to a supersaturated solid solution of nitrogen in α -iron, as there is no loss of nitrogen to the atmosphere in the milling vessel (Table 2).

{Place Fig. 1 about here}

However, the non-detectability by XRPD of a given phase after extended ball milling does not constitute an unambiguous proof of its absence, because, due to the extreme diffraction-line broadening, the reflections of severely deformed material can become indistinguishable from the background signal [1]. In order to resolve this ambiguity, an additional diffraction pattern (Fig. 2) was recorded from a mechanical mixture of 40 h *separately* milled pure α -iron and a 40 h *separately* milled pure ϵ -iron nitride powder, in the same weight ratio as for the initial powder pertaining to Fig. 1 (i.e. milled in the *mixed* fashion). In this case, the reflections of the ϵ -iron nitride can be discerned clearly. Hence, upon ball milling a mixture of α -iron powder together with ϵ -iron nitride powder, the nitride phase dissolves, and an apparently supersaturated solid solution of nitrogen in α -iron remains.

After 40 h of milling a steady state with respect to phase composition (single-phase supersaturated N-ferrite) as well as microstructure (no further change of diffraction-line broadening) is reached. Results analogous to those presented here for sample A5 were obtained for all milling experiments performed with all samples with different weight ratios of α -iron and ϵ -iron nitride; i.e. up to a total nitrogen content of 15.6 at% nitrogen in the steady-state product (Table 2, Fig. 3). For samples with higher nitrogen content, ϵ -iron nitride was detected additionally to the supersaturated ferrite. It strikes that the upper limit of about 16 at% nitrogen for supersaturated N-ferrite is about equal to the lower limit of nitrogen content for ϵ -iron nitride at elevated temperatures (see phase diagram in Ref. [24]).

{Place Fig. 2 and 3 about here}

3.3 Microstructural imperfection

From the broadening of the reflections of the N-ferrites (additional to the instrumental resolution), reaching a steady state after 40 h of milling, information on the microstructure as function of the total nitrogen content can be obtained. One method suitable to characterize and quantify the crystallite size and microstrains is the method proposed by Williamson and Hall [4,30]. If the broadening is solely caused by variations in d-spacing (lattice distortions, dislocations, compositional variations), the effective mean microstrain, e (to be interpreted as a measure for the standard deviation of the microstrain distribution [31]), is given by the integral breadth of the reflection with the Laue indices hkl

$$\beta_{e,hkl} = 4e \tan \theta_{\max,hkl}, \quad (1)$$

where $\theta_{\max,hkl}$ is the peak position (e.g. peak-maximum position). If the broadening originates solely from a reduction of the size of coherently diffracting domains (reduction of crystallite size, stacking faults, twins) the integral breadth of the reflection hkl is given by

$$\beta_{D,hkl} = \frac{\lambda}{D \cos \theta_{\max,hkl}}, \quad (2)$$

where D is the mean size of the coherently diffracting domains and λ is the wavelength. According to the Williamson-Hall analysis, both contributions to the total broadening add linearly (which holds exactly if the line-broadening contributions are of Lorentzian shape) and one obtains for the total physical (size and strain) broadening (integral breadth β_{hkl}):

$$\frac{\beta_{hkl} \cos \theta_{\max,hkl}}{\lambda} = \frac{1}{D} + \frac{4e \sin \theta_{\max,hkl}}{\lambda}. \quad (3)$$

Plotting $\frac{\beta_{hkl} \cos \theta_{\max,hkl}}{\lambda}$ vs. $\frac{4 \sin \theta_{\max,hkl}}{\lambda}$ should yield a straight line with a slope providing a value for e and an ordinate intercept providing a value for $1/D$ (Figs. 4, 5a/b). The values for $1/D$ thus obtained for the N-ferrites (using the 110, 211 and 220 reflections and leaving out the weak 200 reflection) increase largely linearly with total N content, while e exhibits a non-linear dependence on nitrogen content: an increase up to medium nitrogen content, followed by a decrease in microstrain broadening to virtually nil.

{Place Figs. 4 and 5 about here}

3.4 Crystal structure analysis

An increase of the amount of interstitially dissolved nitrogen in α -iron leads to an increase of the lattice parameter of α -iron. The relation between nitrogen content and lattice parameter has been well investigated for solid solutions of nitrogen in α -iron within the small equilibrium homogeneity range [25, 26]. It has also been shown that the increase in volume per iron atom with nitrogen content is given by the same linear dependence for α' -nitrogen martensite and ϵ -iron nitrides (for nitrogen contents less than 33 at.%) [32]. It is questioned whether these dependencies also hold for ferrites of large nitrogen supersaturation as produced by ball milling.

In the present investigation, the positions of the maxima of four reflections (110, 200, 211 and 220) were determined and the corresponding d-spacings were calculated (Fig. 6a). These values obtained for d_{hkl} as function of hkl are clearly incompatible with a single cubic lattice parameter a : hkl -dependent lattice parameters occur, which can be described by

$$a_{hkl} = d_{hkl} \sqrt{h^2 + k^2 + l^2} \quad (4)$$

where a_{hkl} can be called “apparent lattice parameter”, similar to an approach in an other case where anisotropic reflection shifts occurred [33]. With increasing nitrogen content a_{110} , a_{211} , a_{220} increase to different degrees (i.e. the reflection positions shift to lower values of 2θ), whereas a_{200} decreases (i.e. the reflection position shifts to higher values of 2θ). In case of initially pure iron (0.77 at% N), the effect is very small, but detectable. A possible interpretation of the occurrence of the apparent lattice parameter and its dependencies on 2θ and nitrogen content is given in section 4.

{Place Fig. 6 about here}

Mössbauer spectra of samples A2, A5 and A6 resemble closely those published for a similar case [9] and clearly differ from Mössbauer spectra recorded for Fe-N martensite (α') [34], as shown in Fig. 7. This difference of the ball-milling product, nitrogen ferrite, and nitrogen martensite is emphasized by the results of ageing (at temperatures between 100 and 200°C): In case of α' , the ordered α'' -Fe₁₆N₂ nitride phase appeared, whereas for supersaturated nitrogen ferrite, the γ' -Fe₄N phase appears [35].

Data concerning the distribution of N interstitials, in terms of the iron environments, in the ball-milled supersaturated nitrogen ferrite were obtained by numerical fitting of the Mössbauer spectra on the basis of least-squares fitting adopting a Lorentzian peak-shape function corresponding to absorption peaks as obtained for thin absorber conditions.

1
2
3 Statistically acceptable results were obtained on the basis of 7 sets of 6 peaks corresponding
4 to 7 different magnetic states of iron atoms and with an additional single peak close to 0 mm
5
6
7 s^{-1} velocity corresponding to the clearly paramagnetic or super-paramagnetic peak revealed by
8
9 the experimental spectra. Similar results were obtained for samples A2 to A6; results for
10
11 sample A5 are shown in Fig. 7.
12

13 {Place Fig. 7 and Table 3 about here}
14
15
16
17

18
19
20
21
22 Different iron environments correspond to different domains of hyperfine parameters.
23
24 In agreement with Ref. [9], distinction of iron environments can be based mainly on the
25
26 hyperfine magnetic field H . Three domains Δ_i of H defined by 32 – 36 T, 27 – 31 T and 23 –
27
28 26 T have thus been distinguished and identified as due to iron atoms with 0, 1, 2 N interstitial
29
30 neighbours Fe_0, Fe_1, Fe_2 ; their relative abundances, P_i , have been indicated in Table 3.
31
32

33
34 In contrast with the environments Fe_0, Fe_1, Fe_2 , for which a reasonable interpretation
35
36 of the interstitial neighbourhood is possible, interpretation of the iron environment
37
38 corresponding to the central single peak is uncertain. This central single peak most likely is
39
40 caused by small domains of paramagnetic phases such as austenite (the isomer shift of -0.05
41
42 $mm\ s^{-1}$ is comparable with the value obtained for the most symmetrical site of FeN austenite,
43
44 -0.1 $mm\ s^{-1}$) or zones close to lattice defects for which some nitrogen segregation may have
45
46 taken place, therefore the corresponding mean environment is referred to as Fe_n with $n = 3 \pm$
47
48
49
50
51 1.
52

53 Due to the six-fold coordination of N by Fe in an octahedral interstitial site of the bcc-
54
55 Fe lattice, the following relation between the relative abundances P_i of the environments Fe_i
56
57 ($0 \leq i \leq 6$) and the nitrogen/iron atomic ratio y of the supersaturated ferrites holds:
58
59

$$y = 1/6 \cdot \sum_i P_i \cdot i \quad (5)$$

1
2
3 Taking the data from Table 3, it thus follows $y = 0.112 \pm 0.01$, i.e. 10.1 at% nitrogen, which
4 agrees reasonably well with the N content of sample A5 as given by the α -Fe and ϵ -Fe₃N_{1.08}
5 powder fractions and proved by chemical analysis (Table 2). A comparison of the Mössbauer
6 site abundances with those corresponding to a binomial distribution (see Table 3) shows that
7 the occupation of interstitial sites by N atoms in the supersaturated ferrite does not occur
8 completely disorderedly.
9

10 High-resolution transmission-electron microscopy of samples A1 (nearly pure iron;
11 0.77 at% nitrogen) and A4 (10.8 at% nitrogen) confirms a main result of the line-broadening
12 analysis (section 3.3): the crystallite size decreases with increasing nitrogen content. This can
13 be directly concluded from the high-resolution images and the selected-area diffraction (SAD)
14 patterns, where for both samples an electron-diffraction pattern was taken from an area of the
15 same size (Fig. 8). In case of the pure iron sample single spots corresponding to several
16 individual crystals are discernible, whereas in case of the nitrogen-rich sample, reflection
17 spots from a much larger number of very small, randomly oriented crystallites are
18 superimposed and give rise to the formation of diffraction rings.
19
20
21
22
23
24
25
26
27
28
29
30
31
32
33
34
35
36
37

38 The analysis of the high resolution images is difficult due to (i) the small crystallite
39 size, which frequently leads to overlapping of crystallites of different orientations in the
40 viewing direction, and (ii) the severe lattice distortions.
41
42
43
44

45 In one case, for the nitrogen-rich sample, a specific orientation relationship between
46 adjacent crystallites could be observed: $\{1\bar{1}0\}_{bcc1} \parallel \{110\}_{bcc2}$ and $\langle 111 \rangle_{bcc1} \parallel \langle 001 \rangle_{bcc2}$, see
47 Fig. 9. Also, as an unfrequent observation, a crystallite adjacent to grain 2 is visible in Fig. 9,
48 which obviously has a fcc structure with the orientation relationship: $\{110\}_{bcc2} \parallel \{1\bar{1}1\}_{fcc}$ and
49 $\langle 001 \rangle_{bcc2} \parallel \langle 110 \rangle_{fcc}$.
50
51
52
53
54
55
56
57
58
59
60

{Place Figs. 8 and 9 about here}

4. Interpretation of results

4.1 Steady state for crystallite size and microstrain as function of nitrogen content

The crystallite size upon ball milling is determined in general by two competing processes: formation of grain boundaries by breakage and rewelding of crystallites or dislocation rearrangement on the one side and dynamic recrystallization on the other side [36]. The results from the Williamson-Hall plots (Figs. 5a,b) and the HRTEM investigations (Figs. 8, 9) show that the steady-state (ferrite) crystallite size after 40 h of ball milling decreases with increasing nitrogen content of the ferrite. This can be explained as follows. The strong decrease of the eventual mean value of D with increasing nitrogen content indicates that nitrogen stabilizes the grain boundaries and thereby hinders dynamic recrystallization. Additionally, segregation of nitrogen at defects in the bulk {footnote: Segregation of interstitial atoms to one- and/or two-dimensional crystal defects contributes to an apparent enhancement of the solubility of nitrogen in α -iron [37] or in ferritic Fe-Me (Me = e.g. Cr, Mo, V, Ti) systems [38], but to a very much smaller extent as in case of the present supersaturated N-ferrites produced by ball milling} (as dislocations and, in particular (see section 4.2.3), stacking faults) restricts dislocation mobility (solid-solution hardening) and thereby increases the brittleness, promoting breakage of the crystallites.

The variation of microstrain e with nitrogen concentration, Fig 5b, may be ascribed to a variation of the yield limit (or hardness). The increase in yield limit, and thus consequently, an increase of the observed value of microstrain e , with increasing nitrogen content, here up to about 7 at% N, is caused by (i) nitrogen-induced solid solution hardening and (ii) increased grain-boundary density (cf. Hall-Petch relation). For higher nitrogen contents (here, beyond about 7 at%), the grain size is reduced further (Fig. 5a). Below a critical value of the grain size a breakdown of the Hall-Petch relation can occur: For such small grain sizes, a decrease in yield limit with decreasing grain size has been reported for many metallic systems (so-called inverse Hall-Petch relation) [39]. This effect is attributed to

1
2
3 stress relaxation mechanisms specific for nanosized microstructures which become active and
4
5 replace dislocation glide as predominant mechanism for plastic deformation: grain-boundary
6
7 diffusion, grain-boundary sliding, nano-twinning, formation of intrinsic and extrinsic stacking
8
9 faults [40,46,47]. Hence for a grain size smaller than a critical value, here about 10nm, a
10
11 decrease of microstrain e can occur.
12
13
14

17 **4.2 Occurrence of fcc-type crystallites and special orientation relationships**

18
19 The observation of the orientation relationship $\{1\bar{1}0\}_{\text{bcc1}} \parallel \{110\}_{\text{bcc2}}$ and
20
21 $\langle 111 \rangle_{\text{bcc1}} \parallel \langle 001 \rangle_{\text{bcc2}}$, and the occurrence of a fcc structure with the orientation relationship
22
23 $\{110\}_{\text{bcc2}} \parallel \{1\bar{1}1\}_{\text{fcc}}$ and $\langle 001 \rangle_{\text{bcc2}} \parallel \langle 110 \rangle_{\text{fcc}}$, (see Fig. 9; section 3.4) parallels observations
24
25 made previously for the Fe-C system (pearlitic steel) after severe deformation by high-
26
27 pressure torsion [41,42]. Such data can be an indication of an unconventional deformation
28
29 mechanism operating in nanocrystalline iron-based alloys containing interstitial solute atoms.
30
31 Molecular dynamics simulations [43] for crack-tip regions in nanocrystalline (pure) iron have
32
33 shown that upon loading the local formation of a transitional fcc phase is possible by a shear
34
35 process along the bcc- $\{110\}$ planes, which is basically a bcc-like to fcc structure
36
37 transformation. Upon further shearing, the transitional fcc phase is transformed back to bcc.
38
39 The orientation relationship as predicted by these simulations agrees with the one observed in
40
41 the here discussed HRTEM image (Fig. 9). The presence of nitrogen or carbon stabilizes the
42
43 austenite, fcc phase, which promotes the occurrence of the above indicated deformation
44
45 mechanism.
46
47
48
49
50
51
52
53
54

55 **4.3 Crystallography of supersaturated N-ferrite**

56
57 The shifts of the reflection maxima of the supersaturated N-ferrites as functions of hkl and
58
59 nitrogen content are the most striking observations of this work. Two possible explanations
60

1
2
3 for these phenomena will be discussed here, (i) tetragonal distortion of the bcc unit cell of the
4 supersaturated N-ferrite and (ii) the presence of a certain type of stacking faults.
5
6
7
8
9

10 4.3.1 Tetragonal distortion of the ferrite, bcc unit cell

11
12 The occurrence of a tetragonal distortion of the bcc unit cell was proposed previously as a
13 possible explanation for the observed asymmetric nature of the line broadening [15-19] (a
14 systematic hkl -dependence of the shifts of the reflection maxima was not reported in these
15 works). This tetragonal distortion would be realized by preferential occupation by nitrogen of
16 only one type (of three types) of octahedral interstices; i.e. Zener ordering. However, this
17 ordering process is unlikely already because ball milling generally promotes disorder [1]. The
18 effect can be abandoned in particular on the basis of the following evaluation.
19
20
21
22
23
24
25
26
27
28

29 Tetragonal distortion leads to splitting of the bcc reflections into sub-reflections with a
30 specific intensity ratio (only reflections with $|h| = |k| = |l|$ are not affected by tetragonal
31 distortion). For all-different $|h|, |k|, |l|$ there is a splitting into three sub-reflections (“triplets”)
32 with an intensity ration of 1:1:1, in case of $|h| = |k| \neq |l|$ or $|h| \neq |k| = |l|$, the original bcc
33 reflection splits into two bct (body-centered tetragonal) subreflections (“doublets”) with an
34 intensity ratio of 2:1 (this case would pertain to the four bcc type reflections considered in this
35 work). When reflection broadening is very pronounced, as in case of the supersaturated N-
36 ferrites produced by ball milling, such sub-reflections may overlap, leading to asymmetric
37 pseudo-bcc reflections, whose maxima are shifted with respect to the expected values for an
38 undistorted bcc structure.
39
40
41
42
43
44
45
46
47
48
49
50
51
52

53 To check the validity of the proposal of tetragonal distortion it is reasonable to analyse
54 the measured patterns with reflection groups, each group corresponding to one bcc reflection,
55 representing the split-up sub-reflections (“doublets”) formed by tetragonal distortion. In case
56 of the four reflections analyzed in this work, pairs of pseudo-Voigt functions were fitted to
57 each of the reflection groups taking into account the instrumental broadening, on the basis of
58
59
60

1
2
3 the “fundamental parameters” determined from the LaB_6 measurements (section 2.2). The
4 reflection maxima for each of the sub-reflections in the reflection groups were determined by
5 fitting values for the lattice parameters a and c , determined by fitting *jointly* to all reflections.
6
7 The peak-profile parameters, full width at half maximum (FWHM) and mixing parameter (the
8 asymmetry was set to nil), were fitted *individually* for each sub-reflection. The integral
9 intensity ratios were fixed *for every pair of sub-reflections* (= “reflection group”) to be 2:1
10 (see above), whereas the total (i.e. integral) intensities of the tetragonal doublets were refined
11 independently.

12
13 The results of this refinement procedure for sample A4 are shown in Fig. 10. It is
14 evident that the measured diffraction pattern *cannot* be described on the basis of the fitting
15 results: Neither, the shape of the bcc-110 reflection nor the position of the bcc-211-reflection
16 can be modeled adequately with the concept of tetragonal lattice distortion. Moreover, the
17 bcc-200 reflection could only be described on this basis with physically unreasonably large
18 FWHM values for the bct-002 sub-reflection and the bct-112 sub reflection, see Table 4.
19 Hence, tetragonal lattice distortion does not provide a consistent explanation of the individual
20 peak-maximum shifts and peak shapes. Former suggestions of tetragonal distortion [15-19],
21 on the basis of the line broadening of a single reflection, are untenable.

22
23 {Place Fig 10 and Table 4 about here}

24 25 4.3.2 *Stacking faults including spacing faults on bcc {211}-planes*

26
27 Based on a theoretical framework by Warren [44], Wagner, Tetelmann and Otte calculated the
28 effect of stacking faults on {211}-planes in bcc crystals [45] on the positions of reflection
29 maxima in (X-ray) powder-diffraction patterns. The most important aspect of this model is the
30 recognition that the introduction of such a stacking fault, which is characterized by a
31 displacement of $a/3 \langle 1\bar{1}\bar{1} \rangle$ parallel to the {211}-stacking fault plane, is associated with an

increase in layer spacing at and perpendicular to the stacking fault plane, adopting a hard spheres model for the Fe atoms (this contrasts with stacking faults on $\{111\}/\{001\}$ close-packed planes in fcc/hcp-type structures, respectively, which stacking faults are not associated with lattice-spacing changes). This “spacing fault”, which accompanies the stacking fault, involves the occurrence of specific hkl -dependent shifts of reflection maxima.

The model predicts that the positions ($2\theta_{hkl}$) of the reflection maxima are shifted by the presence of the above described type of layer fault by an amount

$$\Delta 2\theta_{hkl} = -2J'_{hkl} \alpha \varepsilon \tan \theta_{0,hkl}, \quad (6)$$

where $\theta_{0,hkl}$ is the diffraction angle calculated for the cubic lattice parameter a_0 , and where α is the stacking fault probability and ε is the local change in layer spacing between two adjacent $\{211\}$ -layers comprising a stacking fault and is given by

$$\varepsilon = \frac{d_{SF,211} - d_{0,211}}{d_{0,211}}, \quad (7)$$

where d_{SF} is the strained $\{211\}$ -lattice plane spacing at the stacking fault and d_0 is the regular $\{211\}$ -lattice plane spacing (calculated from a_0 , see above). J'_{hkl} is a constant which is characteristic for each hkl and takes into account that reflections in a powder-diffraction pattern can be composed of different sub-reflections corresponding to permutation of hkl indices and which are inequivalent with respect to the type of stacking/spacing faulting. Values for J'_{hkl} are given in Table 5. The “apparent” lattice parameter (cf. Eq. (4)) can be derived from $2\theta_{hkl} = 2\theta_{0,hkl} + \Delta 2\theta_{hkl}$ using Bragg’s law and Eq. (6). It follows

$$a_{hkl} = a_0 (1 + J'_{hkl} \alpha \varepsilon) \quad (8).$$

Comparing the values for J'_{hkl} , which determine the deviation of the apparent lattice parameters from the lattice parameter a_0 , with the trends for the experimentally determined apparent lattice parameters of the supersaturated N-ferrites, shows that the effect discussed can at least qualitatively explain the observations (Fig. 6a).

{Place Table 5 about here}

Values for a_0 and $\alpha\epsilon$ were determined by fitting Eq. (8) to the apparent lattice parameters as observed for the supersaturated N-ferrites: the sum of the squared deviations between experimentally observed apparent lattice-parameter values and the apparent lattice-parameter values calculated from Eq. (8) was minimized by adopting a_0 and $\alpha\epsilon$ as fit parameters.

Comparison of the experimentally determined data (Fig. 6a) and the best fits for the various nitrogen contents (Fig. 6b) shows that some deviations occur, which are mainly caused by an apparent lattice parameter deduced from the 110 reflection that is larger than that deduced from the 220 reflection, which is impossible according to the model used here.

The resulting values for the two fit parameters a_0 and $\alpha\epsilon$ are shown in Fig. 11. Their physical plausibility can be discussed as follows: The lattice parameter a_0 , for the unfaulted cubic ferrite, increases with increasing nitrogen content, but not as strongly as expected by extrapolation the relations given in [25,26] for ferrite with nitrogen contents up to 0.2 at%. This could be due to the segregation of nitrogen at lattice defects, where less dilation is required to accommodate the dissolved nitrogen (tensile strained region at dislocation line; octahedral site at stacking fault larger than in the bulk (see below)).

{Place Fig 11 about here}

The octahedral interstitial sites at the stacking faults are larger than those in the bulk: the distance between the interstitial site and the nearest neighbouring Fe atoms is by 19% larger at a stacking fault; cf. Fig. 12. Hence incorporation of interstitial nitrogen atoms at these octahedral interstices leads to less elastic energy than at octahedral interstices in the bulk. For realization of ideal octahedral symmetry some relaxation of atoms (atomic

1
2
3 shuffling) is needed within the faulted $\{211\}$ -plane, which is likely to occur (see also Fig. 12).
4
5 The existence of this type of stacking faults could not be proven by HRTEM imaging. Best
6
7 visibility is expected in grains with $\langle 211 \rangle$ parallel to the incident electron beam, i.e. then the
8
9 stacking fault is imaged edge-on, but only for two of the six equivalent $\langle 211 \rangle$ directions,
10
11 which orientations practically did not occur in the investigated foils.
12
13
14

15
16
17 {Place Fig 12 about here}
18
19
20
21

22 The parameter $\alpha\varepsilon$ determines the extent of the anisotropic hkl reflection shift (Eq. (8)).
23
24 Its observed increase with increasing nitrogen content (Fig. 11) could be attributed to an
25
26 increase of α , the stacking fault density (probability), and/or to an increase of ε , the increase in
27
28 layer spacing at the stacking fault. It may be suggested that stacking faults in the present
29
30 samples are stabilized by the presence of dissolved nitrogen, as discussed above, which can
31
32 explain the increase of $\alpha\varepsilon$ with nitrogen content. An alternative or complementary
33
34 interpretation of the increase in stacking fault density with increasing nitrogen content could
35
36 be given recognizing the decrease of crystallite size with increasing nitrogen content (Fig. 5a,
37
38 section 4.1): Planar faulting (introduction of stacking faults and/or twins) can replace glide of
39
40 perfect dislocations as predominant plastic deformation mode in nanocrystalline materials,
41
42 which has been observed e.g. for nanocrystalline aluminum, whereas planar faults have not
43
44 been observed in coarse grained aluminum upon plastic deformation [46,47]. Further,
45
46 twinning upon plastic deformation has been observed in different nanocrystalline fcc metals,
47
48 which yields no net macroscopic strain, but is supposed to assist plastic deformation by
49
50 favourable reorientation of grains [48].
51
52
53
54
55
56

57 If the atoms of the bcc crystal would be hard spheres, ε can be estimated to be 0.06
58
59 [45]. Adopting this value of ε , α would be 0.75 in case of the sample of highest nitrogen
60
content in this study, which is unrealistic as the resulting crystal structure would no longer

1
2
3 correspond to a (distorted) overall bcc-crystal structure. Hence, it appears that also ε increases
4
5 considerably with nitrogen content, e.g. to 0.2, which would lead to realistic α values. Such
6
7 increase of ε is compatible, indeed, with the above suggested nitrogen segregation at the
8
9 stacking faults.
10
11

12 13 14 15 **5. Conclusions**

16
17 Extremely supersaturated N-ferrites, with nitrogen contents up to 15.6 at%, can be produced
18
19 by ball milling mixtures of pure iron powder and ε -iron nitride powder. The nitrogen content
20
21 has a strong influence on the values for crystallite size and microstrain attained in the steady
22
23 state (after 40 h of ball milling). A small fraction of fcc-like crystallites occurs for the ball-
24
25 milled iron-nitrogen alloys.
26
27

28
29 The crystallite size decreases with increasing nitrogen content, due to the stabilization
30
31 of grain boundaries by nitrogen segregation, thereby hindering dynamic recrystallization, and
32
33 a more brittle nature of the material promoting fracture of the crystallites.
34
35

36
37 The increase in microstrain broadening up to about 7 at% nitrogen is due to the
38
39 increase in yield limit caused by the nitrogen solute atoms and an increase of grain-boundary
40
41 density. Below a critical value of grain size (occurring for nitrogen content larger than about 7
42
43 at%) a decrease of microstrain is due to a decrease of yield limit caused by a replacement of
44
45 dislocation glide as predominant mechanism for plastic deformation by alternative
46
47 mechanisms.
48
49

50
51 The bcc reflections in the XRPD patterns show characteristic hkl -dependent shifts
52
53 which increase with increasing nitrogen content. Interpretation of these reflection shifts as
54
55 caused by a tetragonal lattice distortion, as proposed previously, is incompatible with the
56
57 experimental results obtained for a series of hkl reflections as well as with Mössbauer spectra.
58
59 The shifts can consistently be ascribed to the occurrence of stacking faults on bcc- $\{211\}$
60
planes, in association with spacing faults.

1
2
3 The occurrence of a stacking-fault density increasing with increasing nitrogen content
4 (i.e. with decreasing crystallite size) and the non-monotonous variation of microstrain with
5 increasing nitrogen content (i.e. with decreasing crystallite size), exhibiting a maximum value
6 at a specific grain size, indicates the breakdown of the classical Hall-Petch relation for
7 describing the mechanical strength of the nanosized microstructure resulting from ball
8 milling.
9
10
11
12
13
14
15
16
17
18
19
20
21

22 Acknowledgements

23 The Authors wish to thank Dr. F. Phillipp and Ms. M. Kelsch from the Stuttgart Center for Electron
24 Microscopy (STEM) at the Max-Planck Institute for Metals Research for TEM analysis
25
26
27
28
29
30
31

32 References

- 33
34
35 [1] C. Suryanarayana, Prog. Mater. Sci. 46 (2001), p.1.
36
37 [2] E. Gaffet and G. Le Caer, *Mechanical Processing for Nanomaterials*, in *Encyclopedia of Nanoscience and*
38 *Nanotechnology*, Vol. 5, H. S. Nalwa (ed.), American Scientific Publishers, Stevenson Ranch, CA, 2004,
39 p.91.
40
41
42 [3] I. Lucks, P. Lamparter and E.J. Mittemeijer, Acta Mater. 49 (2001) p.2419.
43
44 [4] I. Lucks, P. Lamparter and E.J. Mittemeijer: J. Appl. Crystallogr. 37 (2004) p.300.
45
46 [5] P. Lamparter and E.J. Mittemeijer: Int. J. Mater. Res. 98 (2007) p.485.
47
48 [6] C.C. Koch, Nanostruct. Mater. 9 (1997) p.13.
49
50 [7] T. Koyano, T. Takizawa, T. Fukunaga and U. Mizutani, Jpn. J. Appl. Phys. 32 (1993) p.1524.
51
52 [8] J.Foct and R.S. de Figueiredo, Nanostruct. Mater. 4 (1994) p.685.
53
54 [9] R.S. de Figueiredo and J. Foct, Mater. Sci. Forum 179-181 (1995) p.219.
55
56 [10] J. Foct, R.S. de Figueiredo, O. Richard and J.P. Morniroli, Mater. Sci. Forum 225-227 (1996) p.409.
57
58 [11] H. Xu, K.H. He and L.Z. Cheng, J. Magn. Magn. Mater. 174 (1997) p.316.
59
60 [12] T. Saito, J. Appl. Phys. 87 (2000) p.6514.

- 1
2
3
4 [13] K. Sumiyama, H. Onodera, K. Suzuki, S. Ono, K.J. Kim, K. Gemma and Y. Nishi, *J. Alloy Compd.* 282
5
6 (1999) p.158.
7
8 [14] T. Yamaguchi and H. Saihata, *J. Magn. Magn. Mater.* 254-255 (2003) p.20.
9
10 [15] K.J. Kim, K. Sumiyama, H. Onodera and K. Suzuki, *J. Alloy Compd.* 203 (1994) p.196.
11
12 [16] J.C. Rawers, D. Govier and D. Cook, *Scr. Metall. Mater.* 32 (1995) p.1319.
13
14 [17] J.C. Rawers, D. Govier and R.Doan, *Mater. Sci. Eng. A* 220 (1996) p.162.
15
16 [18] A. Munitz, G. Kimmel, J.C. Rawers and R.J. Fields, *Nanostruct. Mater.* 8 (1997) p.867.
17
18 [19] J.C. Rawers, D. Cook and T. Kim, *Phil. Mag. A* 78 (1998) p.965.
19
20 [20] J.M.D. Coey and K.O. O'Donnell, *Mater. Sci. Forum*, 179-181 (1995) p.513.
21
22 [21] G.M. Wang, S.J. Campbell and W.A. Kaczmarek, *Mater. Sci. Eng. A* 226 (1997) p.80.
23
24 [22] Y. Chen, J.S. Williams and G.M. Wang, *J.Appl. Phys.* 79 (1996) p.3956.
25
26 [23] K.H. Jack, *Proc. R. Soc. Lon. A* 208 (1951) p.216.
27
28 [24] H.A. Wriedt, N.A. Gokcen and R.H. Nafziger, *Bull. Alloy Phase Diagr.* 16 (1987) p.159.
29
30 [25] H.A. Wriedt and L. Zwell, *T. Metall. Soc. AIME* 224 (1962) p.1242.
31
32 [26] P. Ferguson and K.H. Jack, *Heat Treatment '81*, the Metals Society, London, 1983, p.158
33
34 [27] A. Leineweber, H.Jacobs, F.Hüning, H. Lueken and W. Kockelmann, *J. Alloys Compd.* 316 (2001) p.21.
35
36 [28] *Topas, General Profile and Structure Analysis Software for Powder Diffraction Data*, V2.0 (Bruker AXS
37
38 GmbH, Karlsruhe, Germany).
39
40 [29] R.W. Cheary, A. Coelho and J.P. Cline, *J. Res. NIST* 109 (2004) p.1.
41
42 [30] G.K. Williamson and W.H. Hall, *Acta Metall.* 1 (1953) p.22.
43
44 [31] R. Delhez, Th.H. de Keijser and E.J. Mittemeijer, *Fresen. Z. Anal. Chem.* 312 (1982) p.1.
45
46 [32] P. Rochegude and J. Foct, *Phys. Status Solidi A* 88 (1985) p.137.
47
48 [33] B. Palosz, E. Grzanka, S. Gierlotka, S. Stel'makh, R. Pielaszek, W. Lojkowski, U. Nismayer, J. Neufeind,
49
50 H.-P. Weber and W. Palosz, *Phase Transit.* 76 (2003) p.171.
51
52 [34] P. Rochegude and J. Foct, *Phys. Status Solidi A* 98 (1986) p.51.
53
54 [35] J. Foct, *Mater. Sci. Forum* 325-326 (2000) p.99.
55
56 [36] J. Eckert, J. C. Holzer, C. E. Krill and W. L. Johnson, *J. Mater. Res.* 7 (1992) p.1751.
57
58 [37] W. Köster and W. Horn, *Arch. Eisenhüttenwesen* 37 (1966) p.155.
59
60 [38] M.A.J. Somers, R.M. Lankreijer and E.J. Mittemeijer, *Phil. Mag. A* 59 (1989) p.353.
[39] C.C. Koch and J. Narayan, *Mater. Res. Soc. Symp.* 634 (2001) B5.1.1.

1
2
3
4 [40] I.A. Ovid'ko, *Int. Mater. Rev.* 50 (2005) p.65.

5
6 [41] Y. Ivanisenko, I. MacLaren, R.Z. Valiev and H.-J. Fecht, *Adv. Eng. Mater.* 7 (2005) p.1011.

7
8 [42] Y. Ivanisenko, W. Lojkowski, R.Z. Valiev and H.-J. Fecht, *Acta Mater.* 51 (2003) p.5555.

9
10 [43] A. Latapie and D. Farkas, *Model. Simul. Mater. Sci. Eng.* 11 (2003) p.745.

11
12 [44] B.E. Warren, *Progr. Met. Phys.* 8 (1959) p.147.

13
14 [45] C.N.J. Wagner, A.S. Tetelman and H.M. Otte, *J. Appl. Phys.* 33 (1962) p.3080.

15
16 [46] M. Chen, E. Ma, K.J. Hemker, H. Sheng, Y. Wang and X. Cheng, *Science* 300 (2003) p.1275.

17
18 [47] X.Z. Liao, F. Zhou, E.J. Lavernia, S.G. Srinivasan, M.I. Baskes, D.W. He and Y.T. Zhu, *Appl. Phys. Lett.*
19
20 83 (2003) p.632.

21
22 [48] X.L. Wu, X.Z. Liao, S.G. Srinivasan, F.Zhou, E.J. Lavernia, R.Z. Valiev and Y.T. Zhu, *Phys. Rev. Lett.* 100
23
24 (2008) 095701
25
26
27
28
29
30
31
32
33
34
35
36
37
38
39
40
41
42
43
44
45
46
47
48
49
50
51
52
53
54
55
56
57
58
59
60

Table 1: Nitrogen and oxygen content of starting materials

	nitrogen content (at%)	oxygen content (at%)
α -Fe	0.04 ± 0.01	1.1 ± 0.03
ϵ -Fe ₃ N _{1.08}	26.7 ± 0.8	1.3 ± 0.1

Table 2: Initial nitrogen content of powder mixtures before milling and final nitrogen and oxygen contents of powders in as-milled state (milling time 40 h). The number between brackets in the column “initial composition” indicates the ϵ -nitride/ferrite weight ratio in the initial powder mixture.

samples	initial composition	as-milled	
	N content (at%) (ϵ -nitride /ferrite weight ratio)	N content (at%)	oxygen content (at%)
A1	0 (0)	0.66 ± 0.02	1.4 ± 0.03
A2	3.4 (0.14:1)	4.4 ± 0.1	2.9 ± 0.1
A3	6.0 (0.25:1)	7.1 ± 0.1	2.1 ± 0.04
A4	11.1 (0.59:1)	10.7 ± 0.2	4.7 ± 0.08
A5	11.1 (0.59:1)	11.8 ± 0.8	2.8 ± 0.40
A6	14.7 (1:1)	15.6 ± 0.2	3.0 ± 0.1

Table 3: Results of evaluating of Mössbauer spectra recorded from sample A5: relative abundance P_i (for comparison: values for a binomial distribution of nitrogen as calculated for the given sample composition (11.8 at% N) have been given in brackets) and the peak width.

Fe	hyperfine field domain	relative abundance	peak's width
environment	Δ_i (T)	[binomial distribution] P_i (%)	(mm/s)
Fe ₀	32 – 36	56 ± 2 [48.6]	~ 0.33
Fe ₁	27 – 31	23.5 ± 1 [35.8]	~ 0.38

Fe_2	23 – 26	18 ± 1 [12.4]	~ 0.58
Fe_n	0	2.5 ± 0.5	~ 0.63

Table 4: FWHM values, as obtained from the refinement procedure on the basis of an assumed tetragonal distortion of the bcc-unit cell, for the different sub-reflections resulting from splitting up the bcc-reflections

hkl_{bcc}	hkl_{bct}	Relative intensity of sub-reflection	FWHM [$^{\circ}2\theta$]
110	110	1	1.69
	101+011	2	2.45
200	200+020	2	4.19
	002	1	9.16
211	211+121	2	5.00
	112	1	30.9
220	220	1	6.45
	202+022	2	11.3

Table 5: Values of J'_{hkl} for bcc-powder reflections hkl as used in Eq. (6) and (8) [44]

hkl	110	200	211	220	310	222	321
J'_{hkl}	+0.208	-0.167	+0.021	+0.208	-0.167	-0.167	+0.048

FIGURES

Fig. 1: X-ray powder diffraction patterns (Mo-K α_1 radiation, $\lambda = 0.70926 \text{ \AA}$) of the initial mixture of α -iron powder and ϵ -Fe₃N_{1.08} powder (weight ratio 1.72:1) and as after various milling times. With increasing milling time, all reflections become substantially broadened. Further, the ϵ -nitride reflections disappear: the ball-milled material can be indexed as of single-phase bcc structure. After 40 h of milling a stationary state is reached with respect to the line broadening and the phase composition. Diffraction patterns have been shifted along the ordinate to facilitate their comparison.

Fig. 2: Comparison of diffraction patterns (Mo-K α_1 radiation, $\lambda = 0.70926 \text{ \AA}$) of (a) a mixture of α -iron powder and ϵ -iron nitride powder (weight ratio 1.5:1), where each powder was ball milled *separately* for 40 h and (b) a mixture of α -iron powder and ϵ -iron nitride powder (weight ratio 1.5:1) ball milled after mixing, i.e. *together*, for 40 hours (sample A5, identical with the diffraction pattern at the bottom of Fig. 1). Whereas in pattern (a) the reflections of the ϵ nitride are still discernable despite of some broadening, they are no longer detectable in pattern (b), where furthermore the reflections of the ferrite are much more broadened than in (a). This demonstrates that in case of milling of α -iron and ϵ -iron nitride powders together, an alloying process has occurred.

Fig. 3: X-ray powder diffraction patterns (Co-K α radiation, $\lambda_{\alpha_1} = 1.78897 \text{ \AA}$, $\lambda_{\alpha_2} = 1.79258 \text{ \AA}$) of the milling products after 40 hours of milling (stationary states). Due to different initial weight ratios of α -iron powder and ϵ -iron nitride powder, the mixed powders have different total nitrogen contents.

1
2
3
4
5
6 Fig. 4: Williamson-Hall plots for the diffraction patterns of the supersaturated N-ferrites (cf.
7 Fig. 3). Only the 110, 211 and 220 reflections were used for the linear fit, because the 200
8 reflections are very weak and exhibit very pronounced broadening, rendering determination of
9 their line-broadening parameters unreliable.
10
11
12
13
14
15
16
17
18
19
20
21
22
23

24
25 Fig. 5: Reciprocal average crystallite size (a) and average microstrain (b), as determined from
26 the Williamson-Hall plots (Fig. 4), versus nitrogen content. The error bars indicate the
27 standard deviations of the ordinate intercepts and slopes, respectively, corresponding to the
28 straight lines drawn in the Williamson-Hall plots.
29
30
31
32
33
34
35
36
37
38

39 Fig. 6: (a) Apparent bcc-lattice parameters as determined from the position of the individual
40 reflections of the supersaturated N-ferrites of various nitrogen contents. (b) Apparent bcc-
41 lattice parameters are determined by fitting of Eq. (4), to the experimental data shown in (a)
42 for the reflections' maxima.
43
44
45
46
47
48
49
50

51 Fig. 7: (a) Mössbauer spectrum taken from sample A5 (11.7 at% N); the black solid line
52 represents the best fit employing 7 sets of 6 peaks corresponding to 7 different magnetic states
53 of iron atoms (represented by dotted lines), with an additional single peak close to 0 mm/s
54 (represented by the dashed line). (b) Mössbauer spectrum of virginal α' -FeN_{0.09} (8.2 at% N;
55 nitrogen martensite) produced by quenching from the austenite-phase field, containing
56 residual austenite [33].
57
58
59
60

1
2
3
4
5
6
7
8
9
10
11
12
13
14
15
16
17
18
19
20
21
22
23
24
25
26
27
28
29
30
31
32
33
34
35
36
37
38
39
40
41
42
43
44
45
46
47
48
49
50
51
52
53
54
55
56
57
58
59
60

Fig. 8: SAD pattern (a) and high resolution image (b) of sample A1 (pure iron) after 40 hours of ball milling; SAD pattern (c) and high resolution image (d) of sample A4 (10.7 at% N) after 40 hours of ball milling.

Fig. 9: High resolution electron microscopy image of sample A4 (10.7 at% N) after 40 h of ball milling. Two neighbouring bcc crystallites (bcc1 and bcc2) exhibit the orientation relationship $\{1\bar{1}0\}_{\text{bcc1}} \parallel \{110\}_{\text{bcc2}}$ and $\langle 111 \rangle_{\text{bcc1}} \parallel \langle 001 \rangle_{\text{bcc2}}$. Furthermore, a crystallite of fcc structure is visible. For each of these three crystallites, a *local* fast Fourier transformation (FFT) of the image has been made to identify the crystal structure and the corresponding zone axis parallel to the incident electron beam.

Fig. 10: Result of diffraction-profile fitting (upper grey line), on the basis of the tetragonal distortion model of the bcc-unit cell, to the measured diffraction pattern of a supersaturated N-ferrite (sample A4, 10.7 at% N). Bottom grey line: difference curve.

Fig. 11: Values for the true lattice parameter a_0 and the product of stacking fault probability, α (left ordinate), and increase in lattice plane spacing at the stacking faults, ε (right ordinate), as deduced from fitting of the stacking-fault model, (Eq. (4)), to the experimental data for the reflections' maxima.

Fig. 12: Schematic representation of a stacking fault on a (211)-plane in iron in a $[1\bar{1}0]$ projection. The light grey atoms have been shifted by $0.5 \cdot [1\bar{1}0]$, i.e. perpendicular to the plane of drawing, with respect to the dark grey atoms. The plane of faulting is represented by the horizontal dashed line. An octahedral site in the undisturbed lattice (bulk) and an

1
2
3 octahedral site at the stacking fault are displayed by the solid lines. The anisotropy of the
4
5 octahedral site in the perfect bcc-lattice is clearly visible (two nearest Fe neighbours in
6
7 $\langle 001 \rangle$ -direction), whereas the octahedral site at the stacking fault is more regular, especially
8
9 when atomic relaxation by atomic shuffling takes place as indicated by the arrows and the
10
11 dotted circles.
12
13
14
15
16
17
18
19
20
21
22
23
24
25
26
27
28
29
30
31
32
33
34
35
36
37
38
39
40
41
42
43
44
45
46
47
48
49
50
51
52
53
54
55
56
57
58
59
60

For Peer Review Only

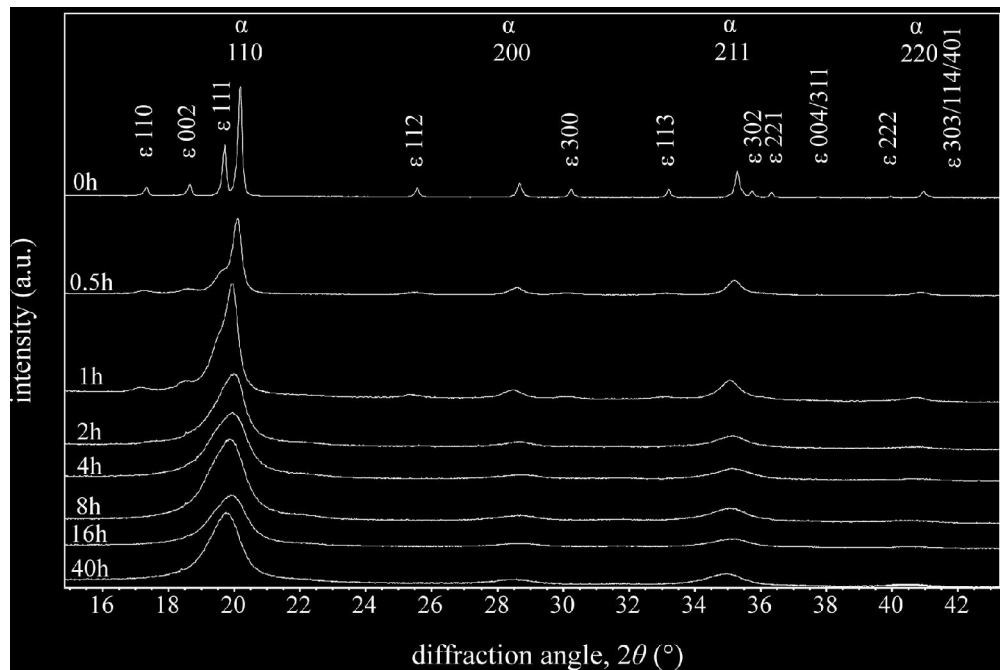
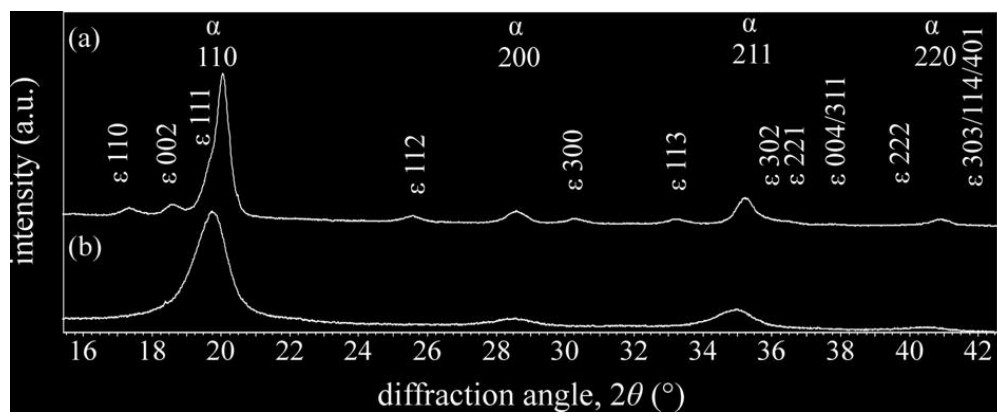


Figure 1
79x52mm (600 x 600 DPI)

**Figure 2**

40x16mm (600 x 600 DPI)

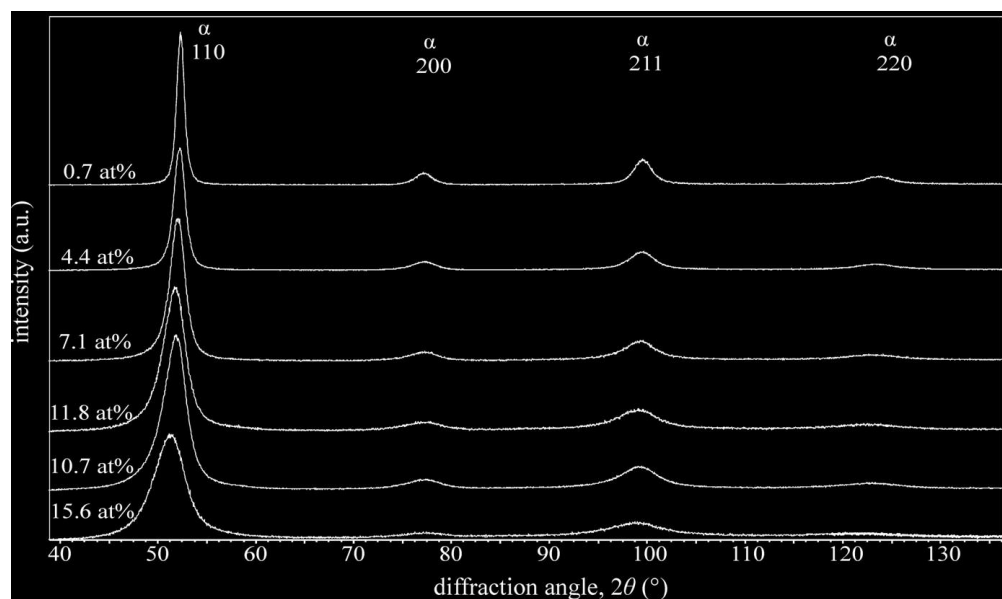
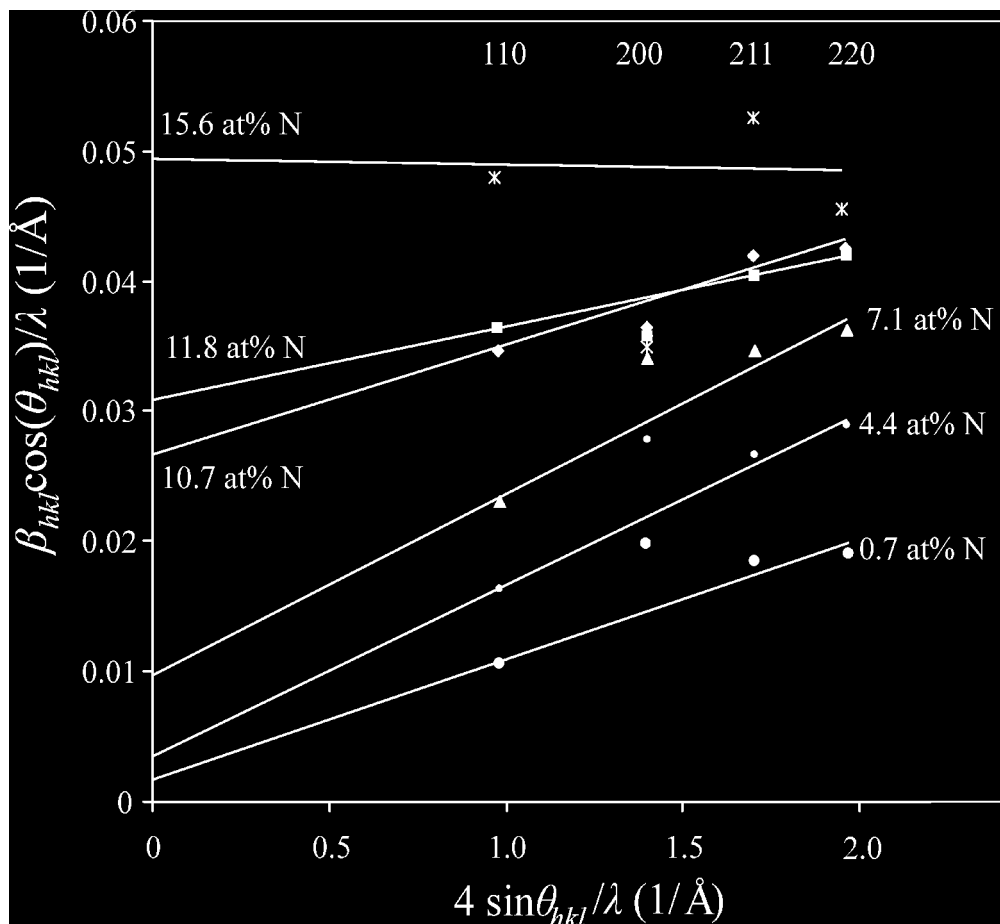
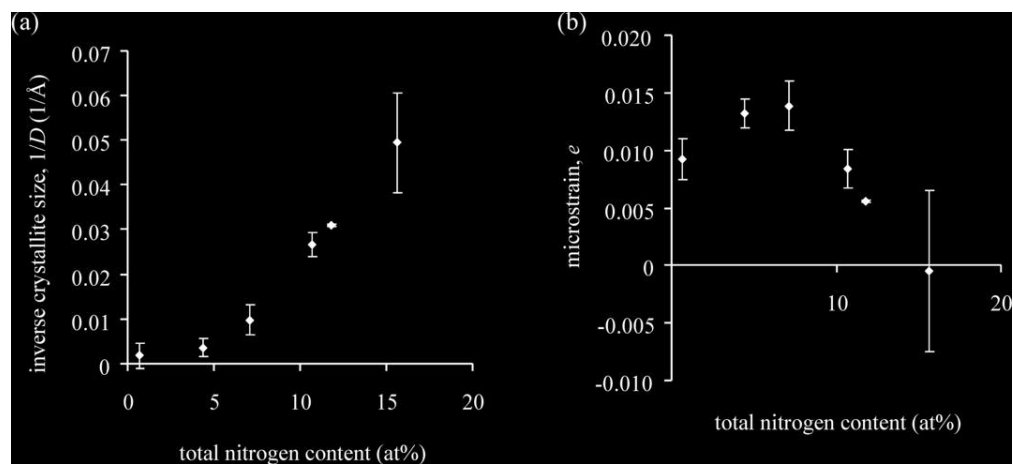


Figure 3
58x34mm (600 x 600 DPI)



148x136mm (600 x 600 DPI)

Only

**Figure 5**

45x20mm (600 x 600 DPI)

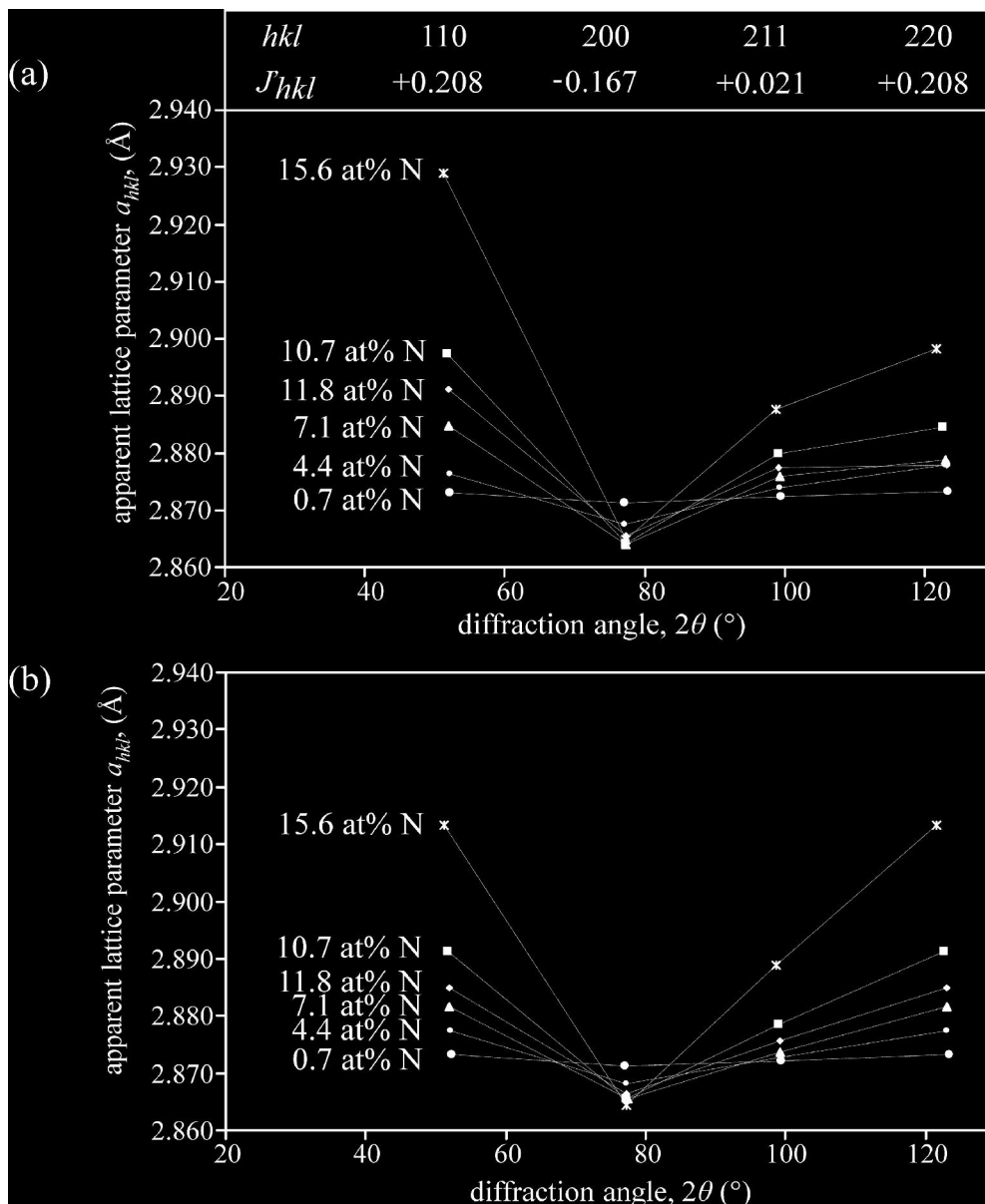


Figure 6
121x146mm (600 x 600 DPI)

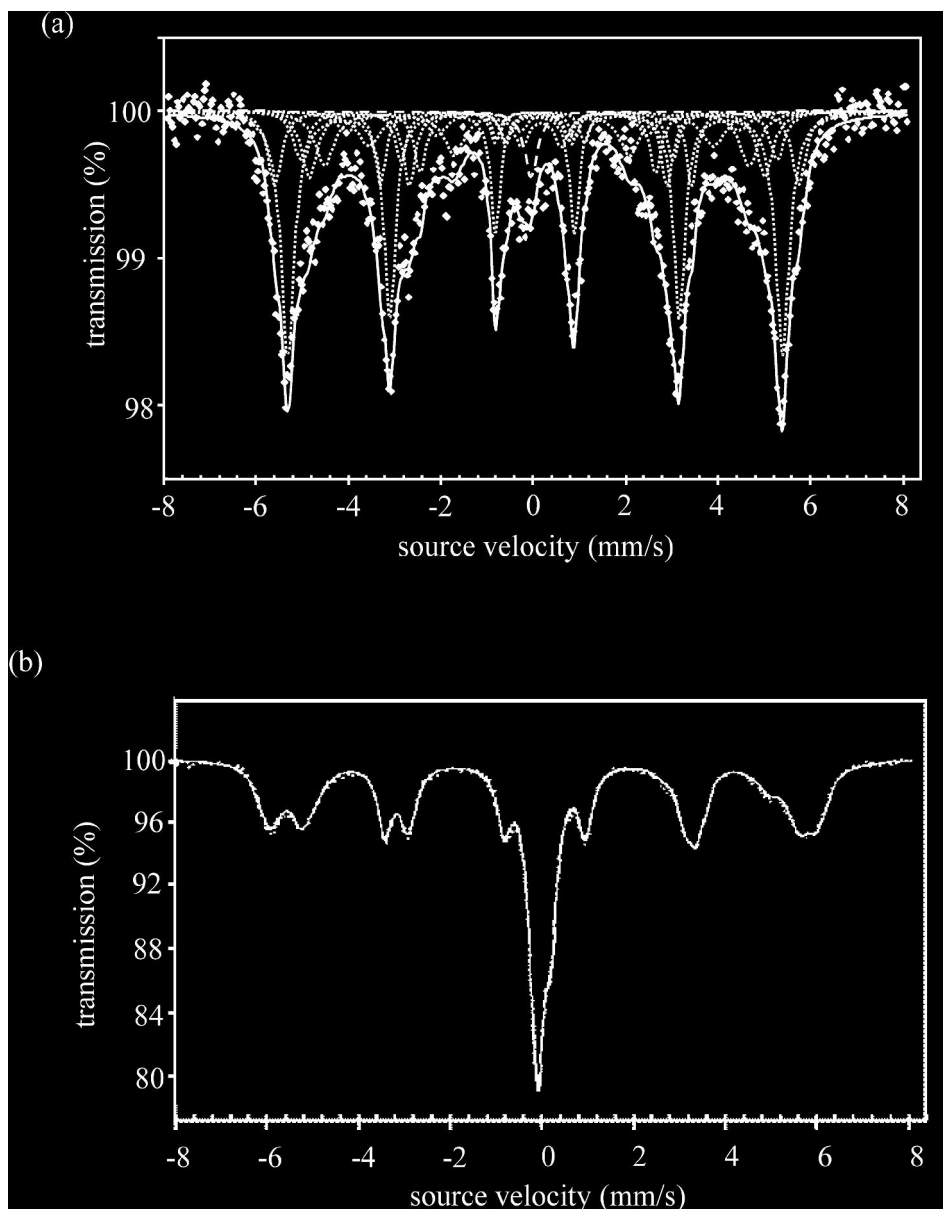


Figure 7
127x161mm (600 x 600 DPI)

1
2
3
4
5
6
7
8
9
10
11
12
13
14
15
16
17
18
19
20
21
22
23
24
25
26
27
28
29
30
31
32
33
34
35
36
37
38
39
40
41
42
43
44
45
46
47
48
49
50
51
52
53
54
55
56
57
58
59
60

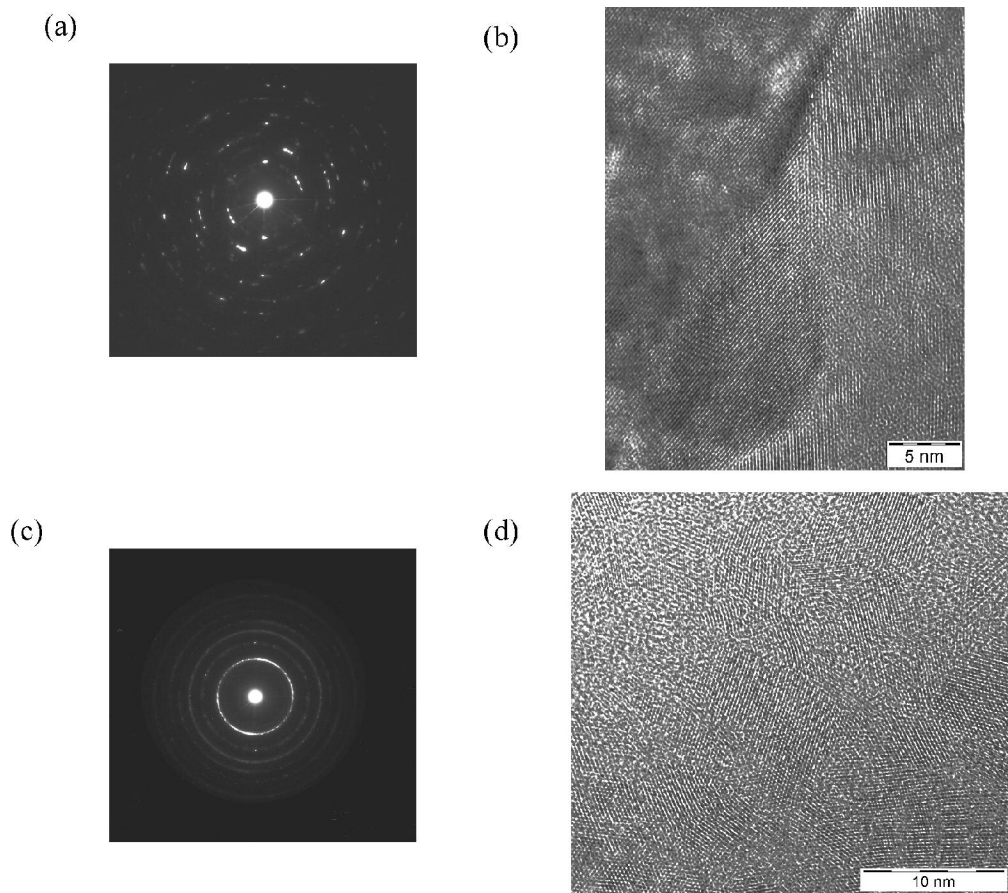


Figure 8
99x88mm (450 x 450 DPI)

Only

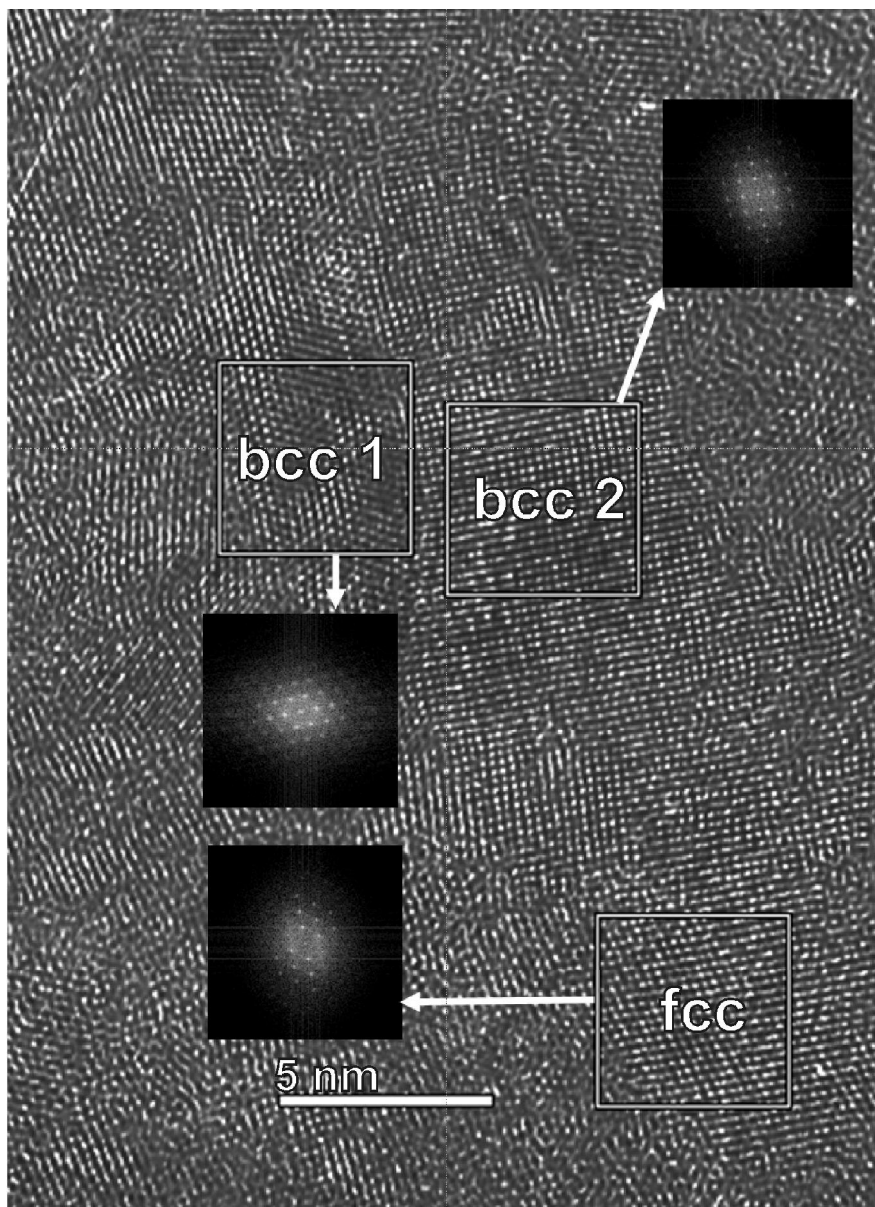
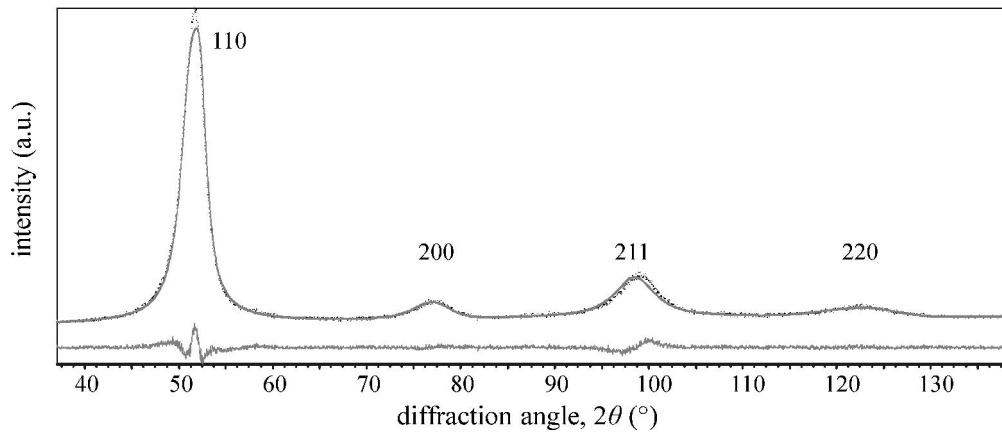
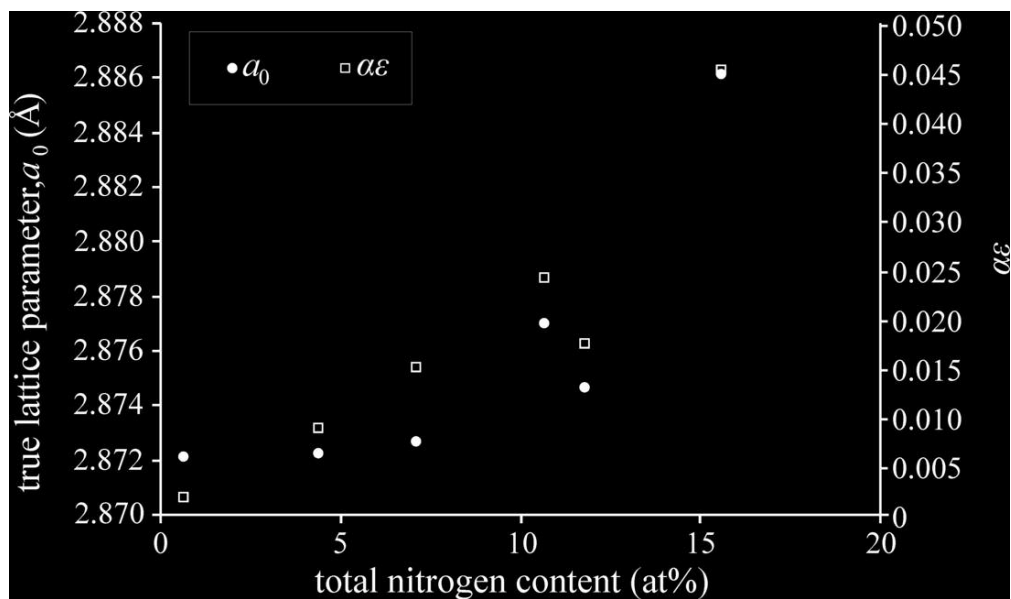


Figure 9
99x136mm (450 x 450 DPI)



132x56mm (600 x 600 DPI)

Peer Review Only



46x27mm (600 x 600 DPI)

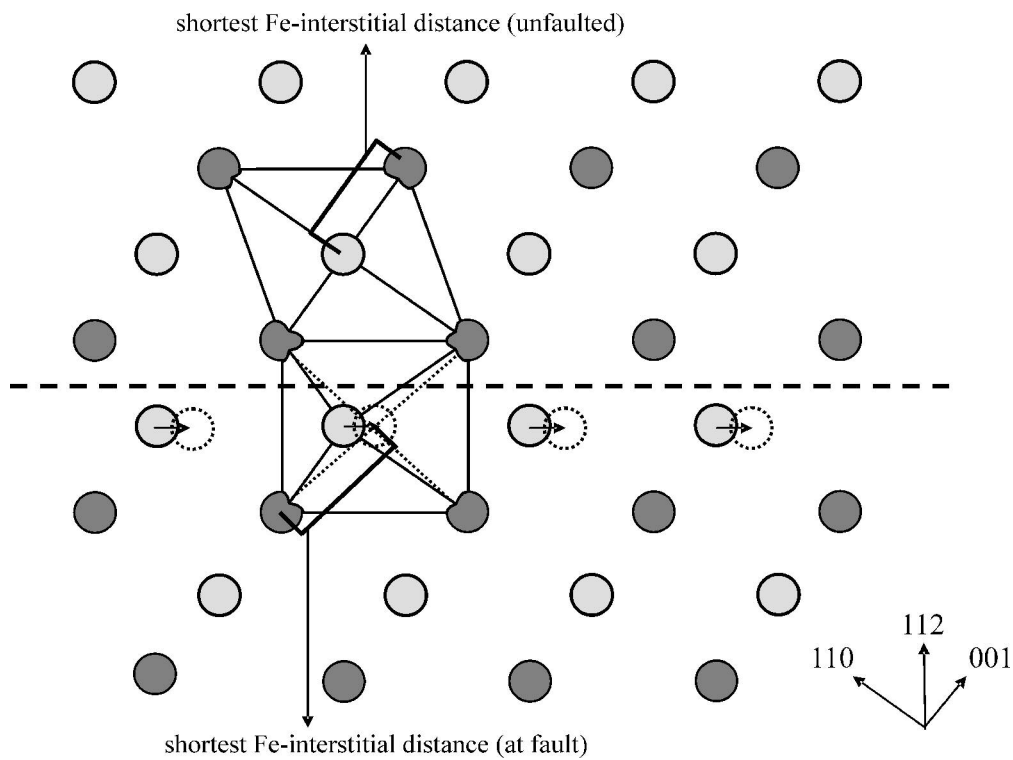


Figure 12
194x145mm (600 x 600 DPI)

Pre-proof Only